SIAM J. MATH. ANAL.
Vol. 21, No. 6, pp. 1511-1536, November 1990

CORRELATIONS BETWEEN CHAOS IN A PERTURBED SINE-GORDON EQUATION AND A TRUNCATED MODEL SYSTEM*

ALAN R. BISHOP†, RANDY FLESCH‡, M. GREGORY FOREST§[1], DAVID W. MCLAUGHLIN¶, AND EDWARD A. OVERMAN, II§[2]

Abstract. The purpose of this paper is to present a first step toward providing coordinates and associated dynamics for low-dimensional attractors in nearly integrable partial differential equations (pdes), in particular, where the truncated system reflects salient geometric properties of the pde. This is achieved by correlating:

(i) Numerical results on the bifurcations to temporal chaos with spatial coherence of the damped, periodically forced sine-Gordon equation with periodic boundary conditions;

(ii) An interpretation of the spatial and temporal bifurcation structures of this perturbed integrable system with regard to the exact structure of the sine-Gordon phase space;

(iii) A model dynamical systems problem, which is itself a perturbed integrable Hamiltonian system, derived from the perturbed sine-Gordon equation by a finite mode Fourier truncation in the nonlinear Schrödinger limit; and

(iv) The bifurcations to chaos in the truncated phase space.

In particular, a potential source of chaos in both the pde and the model ordinary differential equation systems is focused on: the existence of homoclinic orbits in the unperturbed integrable phase space and their continuation in the perturbed problem. The evidence presented here supports our thesis that the chaotic attractors of the weakly perturbed periodic sine-Gordon system consists of low-dimensional metastable attracting states together with intermediate states that are $O(1)$ unstable and correspond to homoclinic states in the integrable phase space. It is surmised that the chaotic dynamics on these attractors is due to the perturbation of these homoclinic integrable configurations.

Key words. chaos, sine-Gordon equation, homoclinic orbits

AMS(MOS) subject classifications. 35B32, 35B35, 58G20

Introduction. The purpose of this paper is to present a first step toward providing coordinates and associated dynamics for low-dimensional attractors in nearly integrable partial differential equations (pdes). In this paper we describe

(i) Numerical results on the bifurcations of the damped, periodically forced sine-Gordon equation with periodic boundary conditions which reveal attractors that are spatially coherent while temporally chaotic;

(ii) An interpretation of the spatial and temporal bifurcation structures of this perturbed integrable system with regard to the integrable structure of the sine-Gordon phase space;

(iii) A model dynamical systems problem, which is itself a perturbed integrable Hamiltonian system, derived from the perturbed sine-Gordon equation by a finite mode truncation in the nonlinear Schrödinger limit; and

(iv) The bifurcations to chaos in the four-dimensional truncated phase space.

* Received by the editors June 16, 1988; accepted for publication (in revised form) December 1, 1989.

† Theoretical Division and Center for Nonlinear Studies, Los Alamos National Laboratories, Los Alamos, New Mexico 87545.

‡ L.A.M.F. Technical University of Denmark, Building 303, DK-2800, Lyngby, Denmark.

§ Department of Mathematics, Ohio State University, Columbus, Ohio 43210.

¶ Department of Mathematics and Program in Applied Mathematics, University of Arizona, Tucson, Arizona 85721. The work of this author was partially supported by National Science Foundation grant DMS 8403187 and Air Force Office of Scientific Research grant AFOSR 830227.

[1] The work of this author was partially supported by National Science Foundation grant DMS 8803465.

[2] The work of this author was partially supported by National Science Foundation grant DMS 8818640 and Air Force Office of Scientific Research grant AFOSR 88-0195. This author acknowledges a grant of computer time from the Ohio Supercomputer Center.

In particular, we focus on a likely source of chaos in both the pde and ordinary differential equation (ode) systems: the existence of homoclinic orbits in the unperturbed integrable phase space and their continuation in the perturbed problem. In the last part of this study, we numerically correlate the homoclinic crossings in the chaotic dynamics of the full and reduced problems.

While the present paper does succeed in revealing homoclinic structure of the pde in a finite mode truncation, we do not claim that this four-dimensional real truncation is sufficient for other important features. On the contrary, two more dimensions are required to accurately cover the attractor [11], to resolve the unstable manifolds of metastable states on the attractors [12], and to quantitatively reproduce the pde bifurcation sequence [11].

These and similar [1], [2] experimental results provide information about

(i) The coexistence of simple coherent spatial structures and temporal chaos;

(ii) The potential for capturing the pde bifurcation sequence with truncated modal systems; and

(iii) The potential for identifying coordinates for chaotic attractors.

These studies also provide directions for the rigorous mathematical analysis to support the numerical work in the individual pde and ode systems, as well as to develop the connections between the full and reduced systems. We discuss some current projects in § 6.

The outline for the remainder of the paper is as follows:

Section 1 gives numerical bifurcations of the perturbed sine-Gordon equation; § 2 gives a truncated two-mode expansion in the nonlinear Schrödinger limit; § 3 gives properties of the unperturbed modal equations; § 4 gives bifurcations of the perturbed modal equations; and § 5 gives correlations between the infinite-dimensional and reduced systems.

1. Numerical bifurcations of the perturbed sine-Gordon equation. We begin by describing one particular experiment from our body of numerical studies (e.g., [1], [2]) on the weakly damped, periodically forced, sine-Gordon equation

$$u_{tt} - u_{xx} + \sin u = \varepsilon[-\alpha u_t + \Gamma \cos(\omega t)], \tag{1.1a}$$

under periodic boundary conditions

$$u\left(x = -\frac{L}{2}, t\right) = u\left(x = \frac{L}{2}, t\right) \quad \text{for all } t, \tag{1.1b}$$

and with even spatial symmetry

$$u(x, t) = u(-x, t) \quad \text{for all } t.$$

For the purpose of this paper we restrict attention to one bifurcation parameter $\varepsilon\Gamma$, the amplitude of the external driver. The remaining parameters are fixed in the following way:

(i) The linear damping coefficient $\varepsilon\alpha$ is chosen very small:

$$\varepsilon\alpha = .04; \tag{1.1c}$$

(ii) The external driving frequency ω is chosen near but less than 1:

$$\omega = 1 - \varepsilon\tilde{\omega} = .87; \tag{1.1d}$$

(iii) The spatial period L is fixed at

$$L = 12; \tag{1.1e}$$

and

(iv) The initial condition is given as a single-hump sine-Gordon breather localized within the period.

With this parameter specification, we observe the following (Fig. 1) long-time asymptotic states as a function of the bifurcation parameter $\varepsilon\Gamma$. The numerical methods used to discretize this pde are discussed in the Appendix. These long-time states, or "attractors," are specified by their spatial structure and temporal behavior, with the notation: K_0 denotes a spatially homogeneous component, of zero wavenumber; K_1 denotes a period one component of wavenumber $K_1 = 2\pi/L$; $K_0 \oplus K_1$ denotes the nonlinear superposition of the two modes, etc. *Locked* implies a frequency-locked state, oscillating at the driven frequency ω. Chaotic denotes a broad-banded frequency spectrum.

This particular bifurcation sequence does not exhibit quasi periodicity prior to chaos, which is a typical route to chaos in other parameter regimes [1], [2]. A more exhaustive parameter study is required to resolve whether stable quasi-periodic attractors occur in this diagram. However, the model problem we present below indicates that when a second frequency is excited at this parameter specification, the collective quasi-periodic state is unstable and thus would not be observed numerically. This structure is reflected in the pde chaotic dynamics in that the system intermittently settles into weakly unstable quasi-periodic states; we illustrate this in Fig. 2, where $\varepsilon\Gamma = .103$.

We emphasize the spatial coherence coexisting with temporal intermittent chaos, and moreover in a parameter range very near the integrable sine-Gordon pde. Fig. 2(a) displays the evolution of the spatial structure in time, beginning at $t = 50{,}000$, long after all transients have passed. Note the intermittent jumping between two weakly unstable spatial structures, a "breather" (localized hump) peaked either at the center or at the ends of the interval, with an intermediate passage through a flat state.

In order to quantify this spatial structure at each timestep t_n, we use a recently developed sine-Gordon spectral code to measure the exact sine-Gordon nonlinear mode content in the field $u^\varepsilon(x, t_n)$. (See [2] for details.) For example, Fig. 3(a) is the sine-Gordon spectrum for an exact K_0 sine-Gordon solution, i.e., a solution of the pendulum: $u = 2\sin^{-1}[ksn(t; k)]$, $0 < k^2 < 1$, with frequency $\omega = .87$, and for a spatial period $L = 12$. These spectral curves are invariant under the exact sine-Gordon flow. The endpoints of curves of spectrum are simple periodic spectra, and are closely related to the action variables in the action-angle linearization of periodic sine-Gordon [6]. The other marked points, denoted by △ or □ *within* bands of spectrum, are double periodic spectra, and these label all closed (degenerate) degrees of freedom. In [3] we

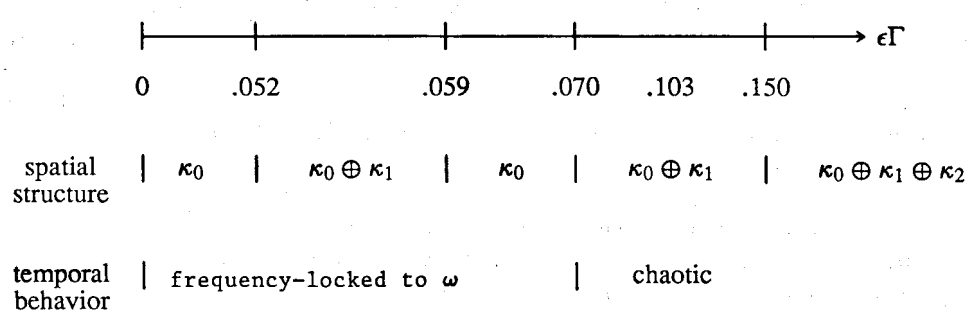

FIG. 1. *The pde bifurcation diagram, corresponding to variable $\varepsilon\Gamma$ with all remaining parameters fixed in equations* (1.1).

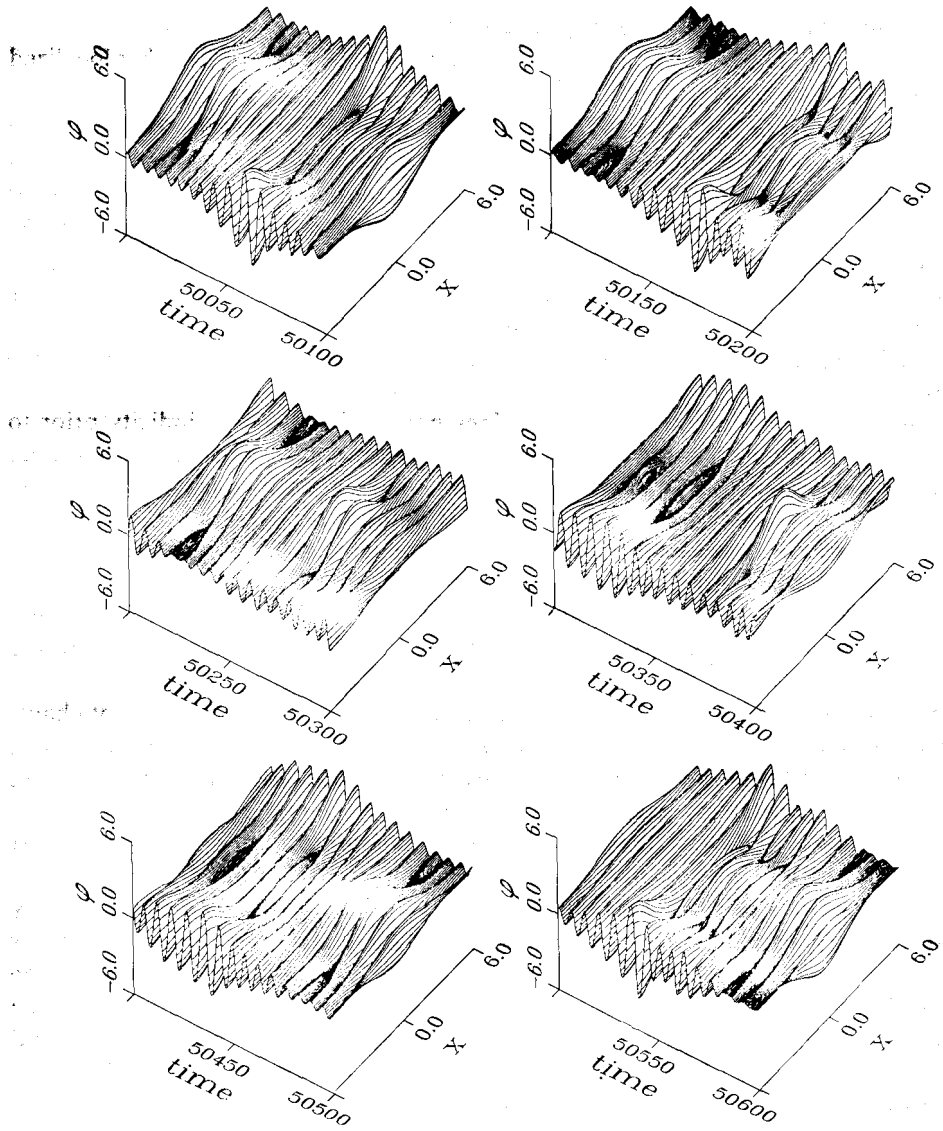

FIG. 2(a). *Numerically computed solution* $\phi = u^{\epsilon}(x, t)$ *of equation* (1.1), $50{,}000 \leqq t \leqq 50{,}600$.

show that there is a 1:1 correspondence between pairs of fully complex (nonreal) double points and linearized, exponentially unstable modes for a given sine-Gordon N degree of freedom solution. Moreover, these local instabilities are reflected globally in the isospectral set of the given solution by homoclinic components. For the example, Fig. 3(a), the number of pairs of complex double points is given by the integer solutions n of $(2n\pi/L)^2 \in (0, k^2)$, where k is the elliptic modulus. Since $L = 12$ here, we find that $n = 1$ is the only solution. The exact K_0 sine-Gordon solution, depicted in Fig. 3(a), with frequency as in (1.1d), on the interval of length $L = 12$,

(i) Is linearly unstable, with order 1 growth rate;

(ii) Has homoclinic orbits on its sine-Gordon isospectral set, which are homoclinic as $t \to \pm\infty$ to this circle (one-torus) of constants in the phase space of L-periodic functions of x; and

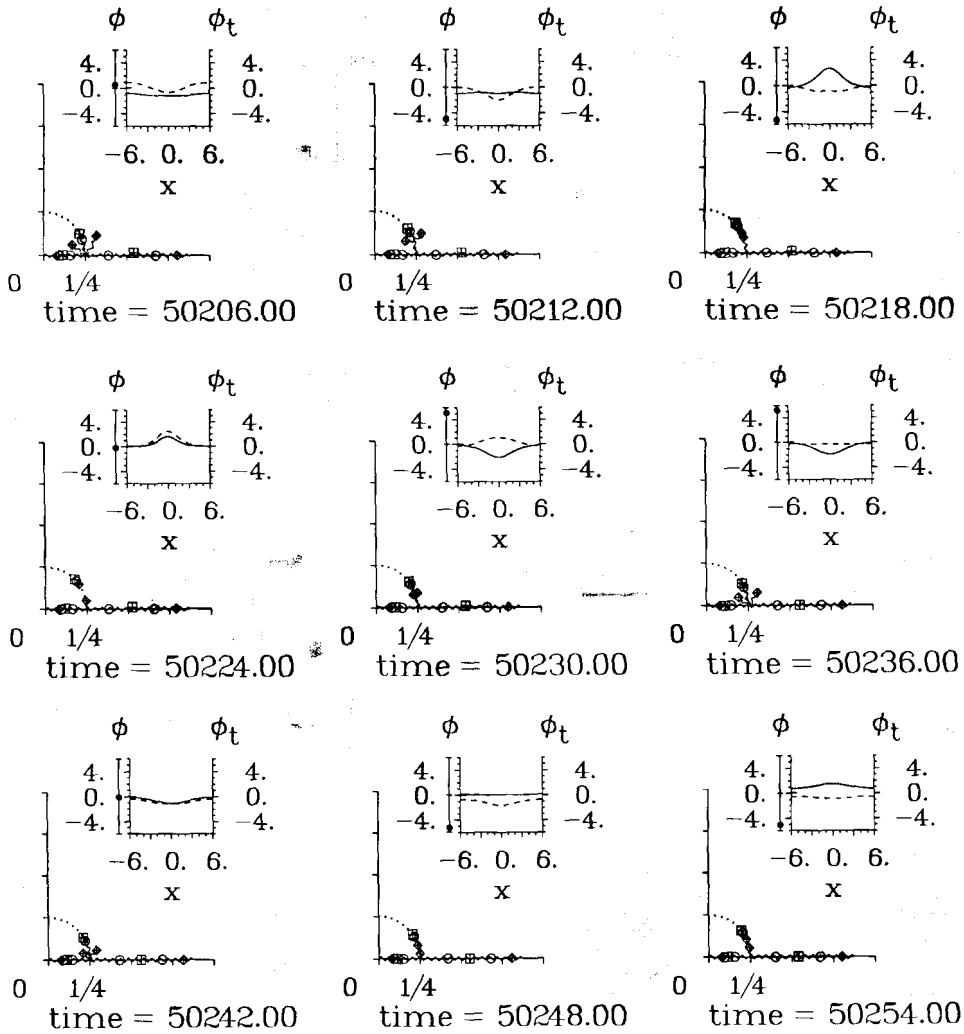

FIG. 2(b). *Corresponding to the numerically computed solution in Fig. 2(a), $\phi = u^{\epsilon}(x, t_n)$ (solid graph) and $\phi_t = (\partial/\partial t)u^{\epsilon}(x, t_n)$ (dotted graph), the sine-Gordon mode projection is numerically measured, with respect to the complex spectral parameter λ, at selected times t_n. (Refer ahead to Fig. 3 for the λ-spectral measurement of three exact sine-Gordon low-mode solutions.) We note: (1) the passage of the perturbed flow from a "cross" spectral projection to a "gap" spectral measurement; and (2) at each discrete time t_n, the spatial waveforms are predominantly nonlinear $K_0 \oplus K_1$ sine-Gordon waveforms.*

(iii) This instability saturates nonlinearly, by arbitrary variation of initial conditions, to the breathers in our following examples [3].

We emphasize that these are low-amplitude spatial structures, far from the amplitude π associated with inverted rest states of the pendulum. These homoclinic orbits of the full pde are thus quite distinct from the separatrices in the x-independent pendulum equation.

The next example is an exact $K_0 \oplus K_1$ sine-Gordon solution: a breather plus nonzero mean. These are *two* such exact nonlinear states (Fig. 3(b)) reflecting the two ways that the degeneracy due to the complex double point in Fig. 3(a) can break. These nonlinear $K_0 \oplus K_1$ states represent exact sine-Gordon solutions, with frequency

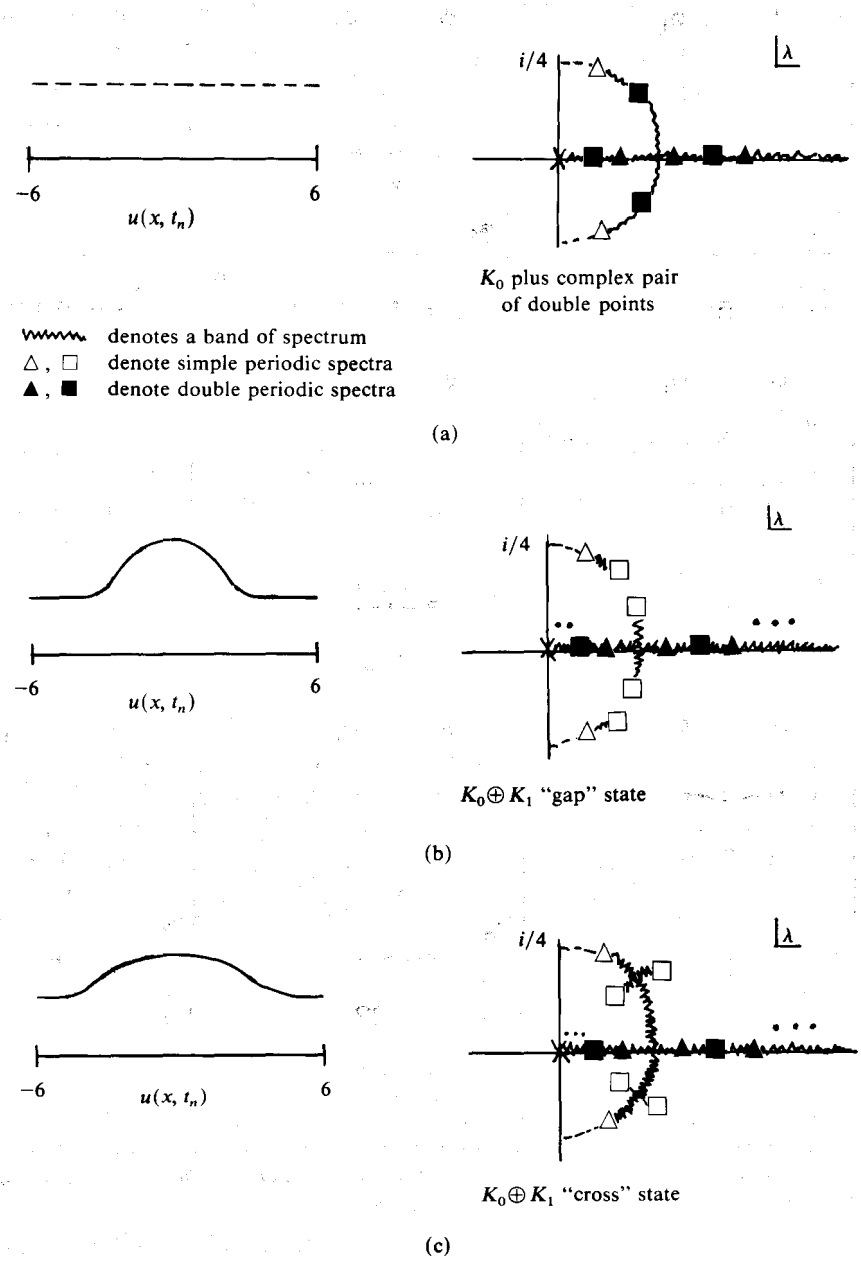

FIG. 3. *A schematic of the spatial structure for three exact sine-Gordon solutions at some discrete time t_n, $u(x, t_n)$, together with the associated λ-spectral measurement. We remark that for exact sine-Gordon flows, the λ-spectral projection is invariant. Fig.* 3(a) *depicts the spectrum of an x-independent pendulum solution which is purely oscillatory in t, with frequency $\omega = .87$, on an x-interval of length $L = 12$. This pure K_0 state has one spectral band on the circle of radius $\frac{1}{4}$, emanating from $\lambda = \frac{1}{4}$, terminating at simple periodic eigenvalues $\lambda = e^{\pm i\psi}/16$, where ψ measures the maximum amplitude of u. For this K_0 solution, on an interval of length $L = 12$, there is one pair of complex conjugate double points which labels the modulational instability of this x-independent solution in the K_1 mode direction. Figures* 3(b) *and* 3(c) *depict pure $K_0 \oplus K_1$ spatial waveforms of sine-Gordon, so-called "breather plus nonzero mean" states. The two spectral configurations represent the two ways the complex double points of Fig.* 3(a) *may break into simple periodic points, opening up order* 1 *amplitude in the K_1 mode, and producing the two types of exact nonlinear $K_0 \oplus K_1$ waveforms.*

$\omega = .87$ as in (1.1d), x-period $L = 12$, and are linearly neutrally stable solutions of the sine-Gordon equation (there are no fully complex double points). Under the unperturbed sine-Gordon dynamics, the spectral configurations in Figs. 3(a) and 3(b) remain invariant.

Under a weakly perturbed flow such as (1.1), initial configurations such as in Fig. 3 will distort due to the perturbation. The endpoints of the spectral curves will modulate, and moreover, the "closed" degrees of freedom will be opened. On short timescales, the neutrally stable modes (associated with real double points) perturb only to the order of the perturbation, whereas the $O(1)$ unstable modes (associated to nonreal double points) generate dramatic changes in spatial structure. Of interest here is which modes resonate with significant amplitude on very long timescales, after all transients have passed, and then how the dynamics of these modes proceed.

At each timestep in the perturbed flow (1.1), we measure the exact nonlinear content in $u^\varepsilon(x, t_n)$, $t_n \gg 1$. In this way we determine if the spatial structure is well approximated:

(1) At a given instant $t_n \gg 1$ by a low degree of freedom exact sine-Gordon field, and

(2) During the flow by a slow modulation through the low-dimensional nonlinear modes, or if the mode content varies widely in a sine-Gordon projection.

Figure 2(b), corresponding to Fig. 2(a), indicates the sine-Gordon mode projection of $u^\varepsilon(x, t_n)$, $t_n \gg 1$, is uniformly very low-dimensional, even in this chaotic regime, and that the energy transfer is predominantly within the nonlinear K_0 and K_1 modes. These measurements quantify our spatial description of the bifurcation diagram in Fig. 1.

Remark. In the Fourier mode projection of $u^\varepsilon(x, t_n)$, a second harmonic $\cos(K_2 x)$ is required to accurately describe the weak instabilities of the (metastable) spatial structures that comprise the chaotic attractor. We refer to [12] for this analysis, and to [11] for a discussion of the truncated Fourier mode system that includes this second harmonic.

The next figure, Fig. 4, is a phase-plane projection of (u, u_t) at one location, $x = 0$, again for $\varepsilon\Gamma = .103$. Another indication of the chaotic dynamics is a broadband power spectrum, which we omit here. (Refer to [1] and [2] for an exhaustive description of the dynamical systems tools which we use to measure the frequency locked, quasi-periodic, and chaotic attractors.)

We close this section with a summary description of the chaotic attractors for (1.1). The dynamics settles into a region of phase space containing two nonlinear $K_0 \oplus K_1$ states (breather plus nonzero mean), with the breather localized in the center of the interval, the other state with the breather translated by $L/2$ to the wings. Note the discrete symmetry due to periodic boundary conditions and symmetric initial data. Each state is "unstable," with weak $O(\varepsilon)$ instabilities due to the perturbation, and the unstable flow out of each state is through a neighborhood of the flat K_0 state, landing either back into the original $K_0 \oplus K_1$ mode, or into the translated $K_0 \oplus K_1$ state. The intermediate K_0 state, however, is unstable (with order 1 growth rate) even in the unperturbed flow, where it has homoclinic orbits associated to it. This apparent random jumping process between the two $K_0 \oplus K_1$ states begs to be identified as a Bernoulli shift on two symbols. In this description the two symbols are identified with the neighborhoods of the two $K_0 \oplus K_1$ states, whereas the perturbed homoclinic structure is responsible for the Bernoulli shift on these symbols.

This phenomenon is the sine-Gordon low-amplitude analogue of the now classical larger amplitude pendulum chaos: the exponentially unstable inverted state ($u = \pi$) which under perturbation has equal likelihood of falling into either of the two states

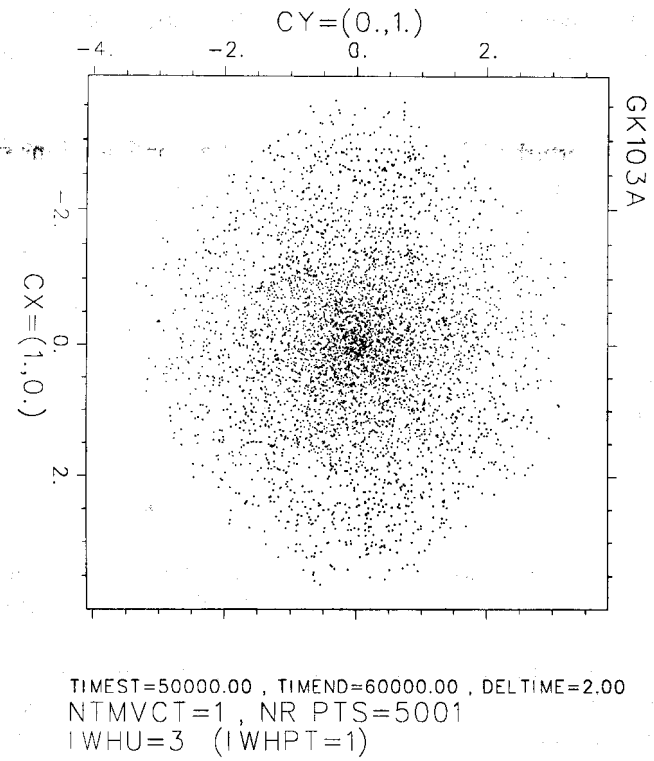

FIG. 4. *The phase plane projection of* (u, u_t) *at* $x=0$, *for the run in Fig.* 2(a), $(u^\varepsilon(0, t_n), u_t^\varepsilon(0, t_n))$, $t_n \in [50{,}000, 50{,}600]$, *with* $\Delta t = 2$.

(oscillatory or running) it separates. These two states are stable in the exact pendulum dynamics, but develop $O(\varepsilon)$ instabilities due to the perturbation, and their perturbed flow often passes randomly through the homoclinic configuration.

Our thesis is that the chaotic attractors of the weakly perturbed periodic sine-Gordon system, e.g., (1.1), consist of low-dimensional metastable attracting states, e.g., the nonlinear $K_0 \oplus K_1$ states of Fig. 2, together with intermediate states that are $O(1)$ unstable and represent homoclinic configurations in the integrable phase space. The chaotic dynamics on these attractors is, we surmise, due to these perturbed homoclinic configurations.

The derivation and analysis of perturbed, fully nonlinear, action-angle modes, truncated on the low-dimensional structures associated to Figs. 2 and 3, are currently under way [5]. As a preliminary step, we develop here a simple model problem that captures some essential qualitative features of this route to chaos in the nearly integrable pde. This model problem is achieved through a natural finite mode truncation on the first two Fourier mode complex amplitudes.

We refer to [11] for a higher mode truncation which is aimed at more accurately covering the chaotic attractors.

2. A truncated finite mode expansion in the nonlinear Schrödinger limit. For frequencies near but less than 1, the weakly perturbed sine-Gordon flow (1.1) resonates with low-amplitude "breatherlike" spatial modes, rather than kink-like modes which can predominate for significantly lower ω [10]. In this limit we easily derive a perturbed nonlinear Schrödinger envelope equation as follows. Seek a solution of (1.1) in the following form (recall $\omega = .87 = 1 - \varepsilon\tilde{\omega}$, (1.1d)):

$$u^\varepsilon = 2\sqrt{\varepsilon\tilde{\omega}}\,[B(X, T)\, e^{i\omega t} + \text{complex conjugate}] + O(\varepsilon), \tag{2.1a}$$

with

$$X=\sqrt{2\varepsilon\tilde{\omega}}\,x, \qquad T=\varepsilon\tilde{\omega}t. \tag{2.1b}$$

Then the slowly varying envelope $B(X, T)$ satisfies

$$-iB_T+B_{XX}+(|B|^2-1)B=i\tilde{\alpha}B+\tilde{\Gamma}. \tag{2.2}$$

From (1.1) the scaled parameters become (approximately):

$$\tilde{\alpha}=\frac{\alpha}{2\varepsilon\tilde{\omega}}\approx .154, \quad L_X=12\sqrt{2\varepsilon\tilde{\omega}}\approx 6.12, \quad k_X=\frac{2\pi}{L_X}\approx 1.025, \tag{2.3a}$$

and the bifurcation parameter $\tilde{\Gamma}$ is now

$$\tilde{\Gamma}=\frac{\varepsilon\Gamma}{8(\varepsilon\tilde{\omega})^{3/2}}\approx 2.67\varepsilon\Gamma. \tag{2.3b}$$

We have achieved two things by reducing to this amplitude equation. First, we preserve the perturbed integrable structure, since the unperturbed pde (2.2) with $\tilde{\alpha}=\tilde{\Gamma}=0$ is the integrable nonlinear Schrödinger equation. Second, we factor out one frequency, ω of the driver. Thus, steady solutions of (2.2) correspond to frequency locked solutions of (1.12), while T-periodic flows of (2.2), incommensurate with ω, correspond to quasi-periodic perturbed sine-Gordon solutions. Chaos in one system is chaos in the other.

We now make a further approximation and truncation based on the predominant $K_0\oplus K_1$ structure measured in Figs. 2 and 3 for the perturbed sine-Gordon flow. (A similar truncation and an interesting numerical study appears in [9]. The primary difference is our focus here on the role of homoclinic structures in the attractors and the comparison with the perturbed pde.) We seek

$$B(X, T)=c(T)+b(T)\cos(kX), \qquad k=\frac{2\pi}{L_X}. \tag{2.4}$$

Inserting this ansatz into the perturbed NLS equation (2.2) and retaining cubic terms in the complex Fourier amplitudes $c(T)$, $b(T)$ yields

$$\begin{aligned} &-ic_T+(|c|^2+\tfrac{1}{2}|b|^2-1)c+\tfrac{1}{2}(cb^*+c^*b)b=i\tilde{\alpha}c+i\tilde{\Gamma},\\ &-ib_T+(|c|^2+\tfrac{3}{4}|b|^2-(1+k^2))b+(cb^*+bc^*)c=i\tilde{\alpha}b. \end{aligned} \tag{2.5}$$

Several remarks about this model four-dimensional dynamical system are appropriate at this point.

Remark 1. This two-complex Fourier mode truncation is surely not expected to yield quantitative agreement with the perturbed pde, although Fig. 3 suggests the two mode $K_0\oplus K_1$ nonlinear truncations provide a very good approximation [5]. This discrepancy in the linear versus nonlinear mode is apparent as we compare a sine-Gordon breather K_1 mode with the Fourier K_1 mode (Fig. 5).

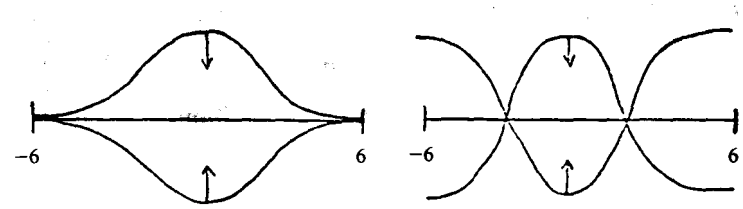

FIG. 5. *Comparison of a nonlinear K_1 breather mode (left) versus a linear K_1 Fourier mode (right).*

Thus, we view this ode system as a model problem and a preview of [5]. Moreover, in [11] we discuss the inclusion of the K_2 Fourier mode into a three-complex mode truncation.

Remark 2. However, this ansatz is capable of modeling some of the apparent features of the perturbed sine-Gordon structure as discussed in § 1. In particular, recall that the chaotic sine-Gordon dynamics (at $\varepsilon\Gamma = .103$, Fig. 3) reflect a competition between a discrete number (here two $K_0 \oplus K_1$) of weakly unstable structures: one with the breather in the center, the other with the breather localized at the ends of the interval. These pde states are, equivalently, related by a half-period translation. Moreover, the pde flow from one state to the other is through the flat K_0 state, which has associated homoclinic orbits in the unperturbed phase space, whereas the unperturbed $K_0 \oplus K_1$ states are neutrally stable in the absence of the perturbation and develop weak instabilities at the onset of chaos.

Now consider the perturbed sine-Gordon solution u^ε, as modeled by this two mode ansatz:

$$u^\varepsilon \sim 2\sqrt{\varepsilon\tilde{\omega}}[(c(T)+b(T)\cos(kX))\, e^{i\omega t}+c.c.]+O(\varepsilon\tilde{\omega}), \tag{2.6}$$

with $c(T)$, $b(T)$ governed by (2.5). These perturbed odes (2.5) admit the symmetry $(c, b) \to (c, -b)$, which is equivalent in u^ε to a translation by $L/2$. Moreover, this symmetry implies that $b = 0$ is an invariant subspace, which for u^ε in (2.6) corresponds to the flat intermediate structure. (The equivalences extend further as discussed in § 3.)

Remark 3. The truncated ansatz (2.6), with c, b governed by (2.5), is robust enough to capture all three spectral configurations of Fig. 3, the $K_0 \oplus K_1$ "gap" state, the $K_0 \oplus K_1$ "cross" state, and the intermediate K_0 state with complex double points and associated homoclinic components, as we will see below. Therefore, this approximation has the potential to flow between gap and cross ($K_0 \oplus K_1$) spectral configurations by passing through the homoclinic K_0 configuration. Recall from Fig. 2(b) and Remark 2 above that this is the spectral flow of the perturbed sine-Gordon equation.

3. Properties of the unperturbed modal equations. In our studies of the perturbed sine-Gordon equation [1], [2], [5], we consistently aim to interpret the perturbed system by projection into the phase space of the integrable sine-Gordon equation. Our understanding of finite-dimensional invariant sets in the exact phase space is the foundation of our studies of the perturbed problem. Consistent with this philosophy, we now describe properties of the unperturbed modal system:

$$\begin{aligned} &-ic_T+(|c|^2+\tfrac{1}{2}|b|^2-1)c+\tfrac{1}{2}(cb^*+c^*b)b=0,\\ &-ib_T+(|c|^2+\tfrac{3}{4}|b|^2-(1+k^2))b+(cb^*+c^*b)c=0. \end{aligned} \tag{3.1}$$

Property 1 (integrable Hamiltonian structure). The two complex- (four real-) dimensional system (3.1) is an integrable Hamiltonian system, with two real independent integrals:

$$\begin{aligned} &I=|c|^2+\tfrac{1}{2}|b|^2,\\ &H=\tfrac{1}{2}|c|^2+|b|^2|c|^2+\tfrac{3}{16}|b|^4-\tfrac{1}{2}(1+k^2)|b|^2-|c|^2+\tfrac{1}{4}(b^2c^{*2}+b^{*2}c^2). \end{aligned} \tag{3.2}$$

The system (3.1) can be placed in complex Hamiltonian form as follows. Let $q_1 = c$, $p_1 = c^*$, $q_2 = b/\sqrt{2}$, $p_2 = b^*/\sqrt{2}$, so that the "energy" H takes the form

$$H(q_1, q_2, p_1, p_2) = \tfrac{1}{2}q_1^2p_1^2+2q_1q_2p_1p_2+\tfrac{3}{4}q_2^2p_2^2-(1+k^2)q_2q_2-q_1p_1+\tfrac{1}{2}(q_2^2p_1^2+q_1^2p_2^2).$$

Then Hamilton's equations with this complex structure are

$$\begin{pmatrix} \mathbf{q} \\ \mathbf{p} \end{pmatrix} = i \begin{pmatrix} 0 & -I \\ I & 0 \end{pmatrix} \nabla_{\binom{\mathbf{q}}{\mathbf{p}}} H,$$

which are precisely equations (3.1) and their complex conjugates.

Property 2 (symmetries). The integrable odes (2.1) admit the following symmetries:

(3.3a) (i) $(c, b) \to (-c, b)$,

(3.3b) (ii) $(c, b) \to (c, -b)$,

(3.3c) (iii) $(c, b) \to (e^{i\phi} c, e^{i\phi} b)$ for any $\phi \in R$.

The reflection symmetries (i), (ii) yield two invariant planes: $c = 0$ and $b = 0$. The S^1 symmetry (iii) yields a circle of fixed points for each nontrivial fixed point.

Property 3 (sets of fixed points). The system (3.1) has three rings of fixed points:

(3.4a) *Ring* 1. $(c, b) = (e^{i\phi}, 0)$, $\phi \in [0, 2\pi)$ in the $b = 0$ invariant subspace;

(3.4b) Ring 2. $(c, b) = \left(0, e^{i\phi} \sqrt{\frac{4}{3}(1+k^2)}\right)$, $\phi \in [0, 2\pi)$, in the $c = 0$ invariant subspace;

(3.4c) *Ring* 3. $(c, b) = \left(e^{i\phi} \sqrt{\frac{1+2k^2}{5}}, 2e^{i\phi} \sqrt{\frac{2-k^2}{15}}\right)$, $\phi \in [0, 2\pi)$.

Remark. For larger lengths $L > 12$, another fixed-point ring exists [11].

The quadrature solution of these integrable equations is most easily affected by the polar coordinate form of (3.1).

Property 4 (polar form of the unperturbed odes). Let $c = C e^{i\gamma}$, $b = B e^{i\beta}$, $\theta = 2(\gamma - \beta)$; then (3.1) becomes

$$\begin{aligned} &C_T + \tfrac{1}{2} C B^2 \sin\theta = 0, \qquad B_T - C^2 B \sin\theta = 0, \\ &\theta_T + (I + 2k^2) - 3C^2 + 2(I - 2C^2)\cos\theta = 0. \end{aligned} \tag{3.5}$$

For completeness, we also list

$$\gamma_T + C^2 - 1 + \tfrac{1}{2} B^2 (2 + \cos\theta) = 0,$$

$$\beta_T + \tfrac{3}{4} B^2 + C^2 (2 + \cos\theta) - (1 + k^2) = 0.$$

By use of the integrals I and H, it is now easy from (3.5) to effect a complete reduction to quadrature solutions of each choice $I = I_0$, $H = H_0$. These general formulas are not the focus of this paper but will be presented elsewhere [4]. Some special cases will be relevant here (see Property 6 below).

Property 5 (stability type for each ring of fixed points). The S^1 symmetry, together with the fact that the amplitudes are constant when $B = 0$ (Ring 1), or $C = 0$ (Ring 2), or $\theta = 0$ (Ring 3), produce a double linearized eigenvalue of zero for each ring. The linearized stability of these fixed points is therefore straightforward to compute; we find:

Ring 1. $(c, b) = (e^{i\phi}, 0)$ has a double zero eigenvalue with associated eigenvectors in the $b = 0$ subspace, and a one-dimensional stable and unstable eigenspace, with $O(1)$ stable and unstable eigenvalues, $\pm k\sqrt{2 - k^2} \approx 1$.

Ring 2. $(c, b) = (0, e^{i\phi}\sqrt{\frac{4}{3}(1+k^2)})$ has a double zero eigenvalue with corresponding eigenvectors in the $c = 0$ subspace, and two purely imaginary, complex conjugate eigenvalues, $\pm i\sqrt{\frac{1}{3}(4k^4-1)}$. These fixed points are purely center-like.

Ring 3.

$$(c, b) = \left(e^{i\phi}\sqrt{\frac{1+2k^2}{5}}, 2\,e^{i\phi}\sqrt{\frac{2-k^2}{15}}\right)$$

has a double zero eigenvalue with corresponding eigenvectors in the $\theta = 0$ subspace, and two purely imaginary eigenvalues $\pm i\sqrt{7}|c||b|$. These fixed points are centers.

Property 6 (homoclinic orbits associated to fixed-point Ring 1). The unstable fixed points on Ring 1, with $c = e^{i\phi}$, $b = 0$, lie on the energy surface $H = -\frac{1}{2}$, $I = 1$. These are the asymptotic states associated to heteroclinic orbits on this energy surface, which correspond to the one-dimensional stable and unstable manifolds of each fixed point on Ring 1.

Using the integrals I and H from (3.2), we find a convenient integral is

$$h = H - (\tfrac{1}{2}I^2 - I),$$

which can be manipulated to find

$$\cos\theta = \frac{2h + B^2(\frac{3}{8}B^2 + k^2 - I)}{B^2(I - \frac{1}{2}B^2)}.$$

Using this formula, the polar equations (3.5), and the values $H = -\frac{1}{2}$, $I = 1$, $h = 0$ appropriate to $(c = e^{i\phi}, b = 0)$, we determine an effective oscillator equation for $z = B^2$:

$$\frac{1}{2}z_T^2 + \left[-\frac{z^2}{32}(z - 8k^2)(7z - 8(2-k^2))\right] = h = 0.$$

The familiar potential energy diagram below (Fig. 6), with energy level $h = 0$, exhibits the infinite-period behavior of $z = B^2 : 0 \nearrow \sqrt{\frac{8}{7}(2-k^2)} \searrow 0$, where $\nearrow$, $\searrow$ denote monotonically increasing, decreasing behavior, respectively.

The remaining formulas for C, γ, β are similarly derived [4]. There are also additional orbits homoclinic to the closed curves nested around Ring 1 in the $b = 0$ invariant subspace (see Property 8).

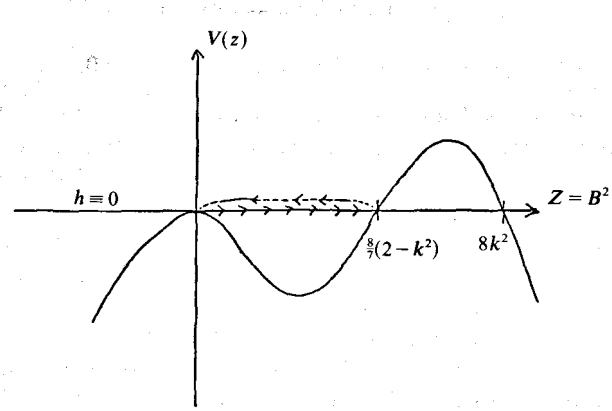

FIG. 6. *Potential energy diagram for* $z = B^2 = |b|^2$.

Property 7 (connection between the ode fixed points and sine-Gordon solutions). In the asymptotic representation (2.6) of sine-Gordon solutions, the above fixed points of the unperturbed odes reflect the following solutions and their stability properties.

Ring 1. $u \sim 2\sqrt{\varepsilon\tilde{\omega}}[c\, e^{i\omega t} + c^* e^{-i\omega t}]$, which corresponds to the K_0 flat pendulum solution, frequency locked to the driver frequency ω. The $O(1)$ instability of these fixed points in the unperturbed system reflects the $O(1)$ instability of the exact K_0 sine-Gordon solution (recall Fig. 3(a) and the surrounding discussion). Moreover, the orbits homoclinic to Ring 1 reflect the sine-Gordon solutions which are homoclinic to the pendulum solution with frequency $\omega = .87$.

Ring 2. $u \sim \sqrt{\varepsilon}[b \cos kX\, e^{i\omega t} + c.c.]$ corresponds to the pure K_1 mode, with a zero-mean (K_0) component, and with frequency of the driver. These solutions exist for sine-Gordon, but are not observed in the perturbed dynamics. This is presumably explained by the larger amplitude of this Ring 2, $|b| \approx \sqrt{8/3}$, relative to the other Rings 1, 3. These corresponding solutions in the perturbed pde would then be expected to show up by varying initial conditions with a significantly larger energy, or by driving the system harder (see § 4).

Ring 3. $u \sim \sqrt{\varepsilon}[(c + b \cos kX)\, e^{i\omega t} + c.c.]$ corresponds to the $K_0 \oplus K_1$ sine-Gordon solution, consisting of the K_1 breather plus nonzero mean, locked at the frequency ω. These states are observed in the perturbed dynamics. Moreover, the unperturbed pde stability type (neutrally stable) agrees with that of the unperturbed odes.

In summary, the fixed-point Rings 1 and 3 in the unperturbed odes reflect remarkably well the unperturbed K_0 and $K_0 \oplus K_1$ sine-Gordon solutions, and moreover maintain a parallel linearized instability and homoclinic orbit structure of the K_0 state, as well as the neutral stability of the $K_0 \oplus K_1$ states.

Below (§ 4) we discuss how the perturbation selects individual points from these rings.

Property 8 (simple periodic orbits nested around the fixed-point rings). The symmetries of the unperturbed odes, Property 2, lead to a nesting of closed curves in the subspaces containing Rings 1, 2, and 3. For example, in the invariant subspace $b = 0$, we find closed curves $|C| = \text{constant} = C_0$, which yields the one-parameter family of periodic solutions:

$$c = C_0\, e^{i(1-C_0^2)T} \quad C_0 = \text{constant}, \qquad b = 0.$$

As $C_0 \to 1$, these curves approach Ring 1 while the frequency goes to zero.

Similarly, in the $C = 0$ invariant subspace there is a one-parameter family of periodic solutions surrounding Ring 2:

$$c = 0, \qquad b = B_0 \exp\left(i(1 + k^2 - \tfrac{3}{4}B_0^2)T\right).$$

In the $\theta = 0$ subspace, which contains Ring 3, we find another one-parameter family of closed curves corresponding to periodic solutions:

$$c = \sqrt{\tfrac{3}{8}B_0^2 + \tfrac{1}{2}k^2} \exp\left(i(1 - \tfrac{1}{2}k^2 - \tfrac{15}{8}B_0^2)T\right),$$
$$b = B_0 \exp\left(i(1 - \tfrac{1}{2}k^2 - \tfrac{15}{8}B_0^2)T\right).$$

Note that these nested closed curves around Rings 1 and 3 are connected at the periodic solution $b = 0$, $c = (k/\sqrt{2}) \exp\left(i(1 - \tfrac{1}{2}k^2)T\right)$. The Floquet stability analysis of these one-parameter families of periodic solutions yields coupled Mathieu equations, to be discussed elsewhere.

4. Bifurcations of the perturbed modal equations. We now discuss how the above properties of the integrable odes (3.1) reveal themselves in the bifurcation structure and dynamics of equations (2.5). Recall that we fix $\tilde{\alpha} = .155$, and consider the bifurcations of (2.5) as the constant driver $\tilde{\Gamma}$ is varied.

The following bifurcation curves (Fig. 7) were originally generated for us by Jolly and Kevrekides using the code AUTO, and since then verified by us, while the linearized eigenvalues and associated eigenvectors were independently computed along the curves by Hyman using the CLAMS package.

We now discuss these bifurcation curves and the associated dynamics.

Property 1 (existence of fixed points as a function of $\tilde{\Gamma}$). Branch *OABFG* is a pure K_0 branch, consisting of steady states with $b = 0$.

Branch *BCD* is a double $K_0 \oplus K_1$ branch, consisting of fixed points (c, b) and $(c, -b)$, with $b \neq 0$, $c \neq 0$. (Recall from Remark 2 in § 2 that the perturbed system (2.5) retains the reflection symmetry $(c, b) \to (c, -b)$, so that all fixed points with $b \neq 0$ come in pairs with equal l_2 norm.) The bifurcation point *B* corresponds both to the change of stability of the K_0 branch of fixed points from one to two unstable dimensions and to the beginning of the $K_0 \oplus K_1$ branch of fixed points.

Some features of this bifurcation diagram are found either analytically or by simple perturbation theory arguments, as we now sketch.

Property 2 (explicit parameterization of the entire K_0 branch of fixed points). With $b = 0$, the fixed points of (2.5) satisfy, with $c = c_1 + ic_2$, $\tilde{\alpha} \approx .155$,

$$\begin{aligned} (c_1^2 + c_2^2 - 1)c_1 + \tilde{\alpha} c_2 &= 0, \\ (c_1^2 + c_2^2 - 1)c_2 - \tilde{\alpha} c_1 &= \tilde{\Gamma}. \end{aligned} \tag{4.1}$$

If we fix $n = \sqrt{c_1^2 + c_2^2} = l_2$ norm of $(c, 0)$, the equations (4.1) represent two orthogonal

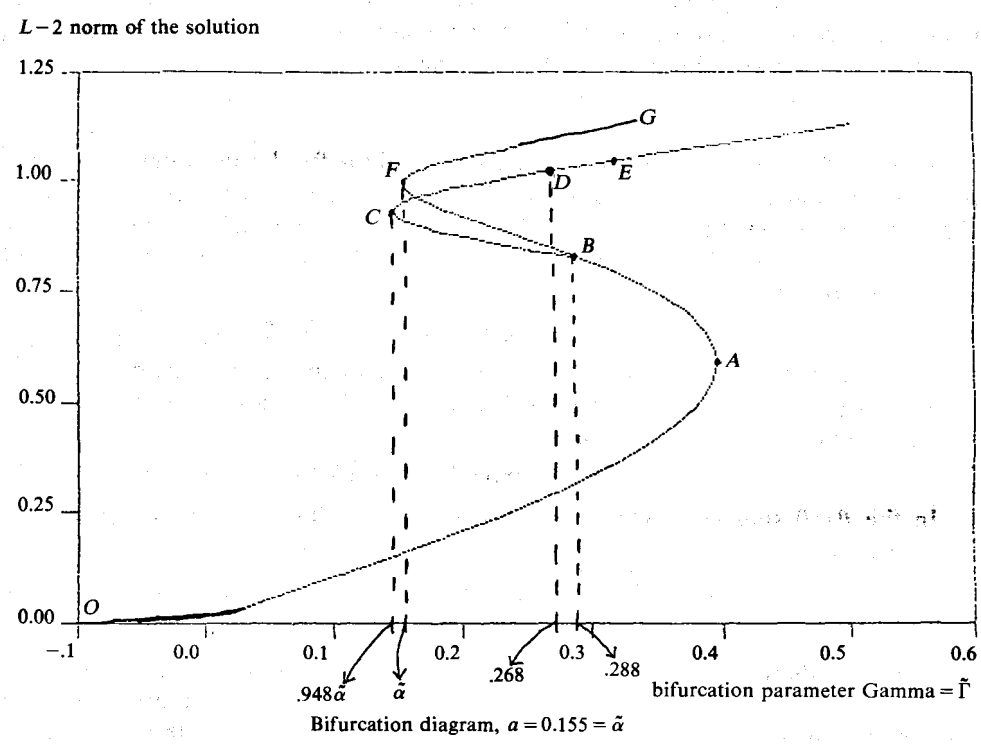

FIG. 7. *Bifurcation diagram of* (2.5) *as* $\tilde{\Gamma}$ *is varied.*

lines in the (c_1^2, c_2^2) plane. We then pick $\tilde{\Gamma}$ such that the two lines intersect on the circle of radius n. This algorithm yields the inverse of the K_0 curve of Fig. 7, which is a nice function:

$$\tilde{\Gamma}(n) = n\sqrt{\tilde{\alpha}^2 + (1-n^2)^2}. \tag{4.2}$$

In this way, we analytically generate the K_0 curve $OABFG$, and calculate the turning points A and F by setting $\tilde{\Gamma}'(n) = 0$, which verifies the numerically generated curve.

Property 3 (perturbation calculations to describe the turning points in the bifurcation branches). By a classical perturbative phase-locking condition, we reproduce the qualitative multibranch structure of Fig. 7, identify these fixed-point branches as phase-locked fixed points from the unperturbed fixed-point Rings 1, 3, and quantitatively capture the turning points or "bends" in the bifurcation curves.

First we compute how the unperturbed integral I varies in the presence of the perturbed dynamics (2.5) (recall that $\tilde{\alpha}$ and $\tilde{\Gamma}$ are our rescaled small parameters):

$$\begin{aligned} \frac{dI}{dT} &= -2\tilde{\alpha}\left[|c|^2 + \frac{1}{2}|b|^2\right] - 2\tilde{\Gamma}\,\mathrm{Re}\,(c) \\ &= -2\tilde{\alpha} I - 2\tilde{\Gamma}\,\mathrm{Re}\,(c). \end{aligned} \tag{4.3}$$

Next we seek fixed points which are perturbations of Rings 1, 2, 3 in (3.4a)-(3.4c) evaluate (4.3) on this ansatz, and demand that dI/dT vanishes to $O(\tilde{\alpha}, \tilde{\Gamma})$—which selects the phase(s) of Rings 1, 2, 3 that "lock(s)" to the perturbation. This procedure yields the following nonresonance or phase-locking conditions:

Ring 1. With $c = e^{i\phi} + \varepsilon\Delta c$, $b = \varepsilon\Delta b$, $0 < \varepsilon \ll 1$, phase-locking criterion: $\tilde{\alpha} + \tilde{\Gamma}\cos\phi = 0$.

Ring 2. With $c = \varepsilon\Delta c$, $b = e^{i\phi}\sqrt{\frac{4}{3}}(1+k^2) + \varepsilon\Delta b$, phase-locking criterion: $\tilde{\alpha} I_0 + \varepsilon\tilde{\Gamma}\,\mathrm{RE}\,(\Delta c) = 0$, where $\mathrm{RE}\,(\,) \equiv$ real part $(\,)$.

Ring 3. With

$$c = e^{i\phi}\sqrt{\frac{1+2k^2}{5}} + \varepsilon\Delta c, \qquad b = 2\,e^{i\phi}\sqrt{\frac{2-k^2}{15}} + \varepsilon\Delta b,$$

phase-locking criterion:

$$\tilde{\alpha}\left(\frac{7+4k^2}{15}\right) + \tilde{\Gamma}^2\cos\phi\sqrt{\frac{1+2k^2}{5}} = 0.$$

This perturbation analysis yields the following conclusions (recall $\tilde{\alpha} = .155$):

Ring 1. $\cos\phi = -\tilde{\alpha}/\tilde{\Gamma}$, so this ring does not phase lock until $\tilde{\Gamma} \geqq \tilde{\alpha}$ (which precisely yields the turning point F), and for $\tilde{\Gamma} > \tilde{\alpha}$ exactly two phases are selected, corresponding to the two branches FG and FB. (The stability of these and other branches is discussed in the next property.)

Ring 2. If $\tilde{\alpha}$, $\tilde{\gamma} = O(\varepsilon)$, there are no solutions of the nonresonance condition $(\tilde{\alpha} I_0 \neq 0)$. However, if $\tilde{\alpha} = O(\varepsilon^2)$, $\tilde{\Gamma} = O(\varepsilon)$, then we find a balance in this equation. This occurs when $\tilde{\Gamma} = O(\sqrt{\tilde{\alpha}})$, which is outside the range of our diagram and so will not be of interest here. (Referring back to § 3, Property 7, Ring 2, we now find these zero-mean solutions do not resonate with the perturbation until the system is driven harder.)

Ring 3. The phase-locking condition yields

$$\cos\phi = -\frac{\tilde{\alpha}}{\tilde{\Gamma}}\frac{7+4k^2}{15}\cdot\sqrt{\frac{5}{1+2k^2}},$$

which correctly predicts the turning point C and the two emanating branches.

Property 4 (stability of the bifurcation branches). In the phase-locked branches of Fig. 7, the upper branches FG and CD locally inherit the stability type of the unperturbed Rings 1 and 3, respectively, while the lower branches FB and CB locally pick up an additional weak unstable eigenvalue due to the perturbation. (These facts are easily deduced perturbatively.)

The stability type of all branches in Fig. 7 is numerically computed, with the following results. Let W_k^s, W_k^u denote a k-dimensional stable or unstable manifold, respectively. Then the following diagram indicates the stability type of each branch: (recall that in dimension four, $W_k^s(\bar{X}_0)$, $W_l^u(\bar{X}_0)$ for hyperbolic fixed points satisfy $k+l=4$, so it suffices to list $W_k^u(\bar{X}_0)$):

Highlights. (1) The K_0 branch FG is the phase-locked continuation branch of Ring 1, which maintains the one-dimensional unstable manifold character of the homoclinic orbits to Ring 1 in the unperturbed problem. The FG branch, therefore, is the perturbed ode signature of the homoclinic pde structures described earlier in § 1.

(2) The double $K_0 \oplus K_1$ branch CD is the stable phase-locked continuation branch of Ring 3, which corresponds in the perturbed pde to the phase-locked, stable, breather plus nonzero mean $(K_0 \oplus K_1)$ solutions.

(3) The point D on the $K_0 \oplus K_1$ branch corresponds to the subcritical Hopf bifurcation. At this value of $\tilde{\Gamma} \approx .268$, the previously stable $K_0 \oplus K_1$ breather plus mean solutions become two-dimensionally, weakly unstable due to the perturbation. As we discuss below, just after this Hopf bifurcation the perturbed system goes chaotic.

Since this Hopf bifurcation is subcritical, the associated periodic orbits of this bifurcation phenomenon are unstable, and these are not observed in our numerical simulations. This fact is quite consistent with the pde bifurcation structure (Fig. 1 and remarks just below it), where in this parameter regime we did not see quasi periodicity

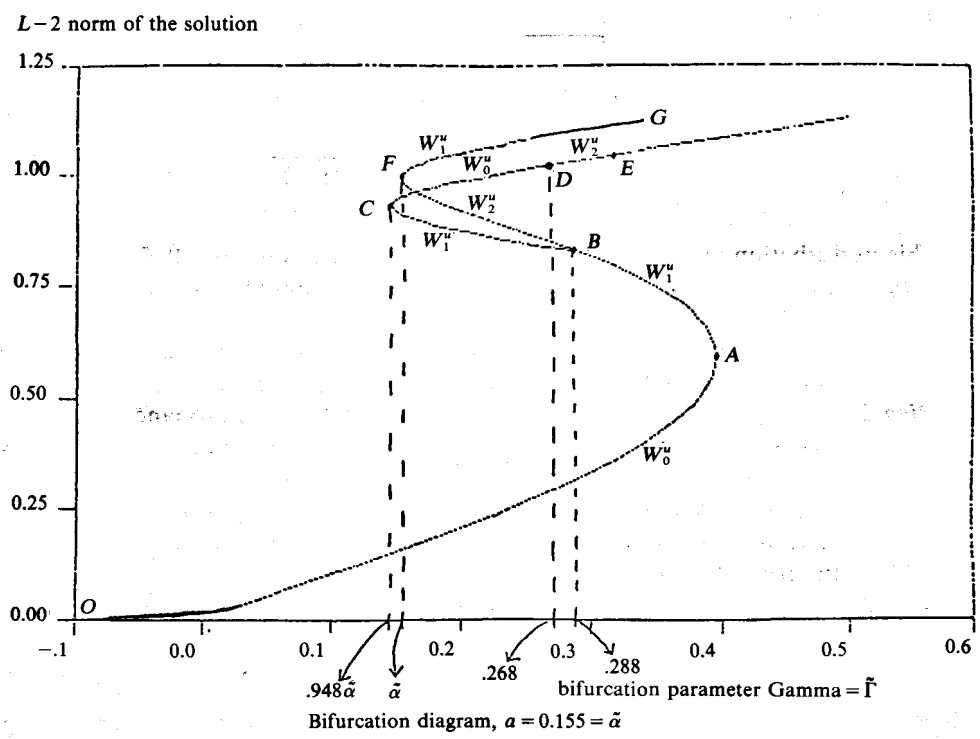

FIG. 8. *Bifurcation diagram with stability type of each branch of fixed points.*

prior to chaos. This model suggests that when the second frequency is generated by Hopf bifurcation in the pde, it is unstable in this specific parameter regime.

Property 5 (global connections between fixed points: before and after the Hopf bifurcation). We have numerically determined the global connections of the unstable manifolds of fixed points at given stress parameter values $\tilde{\Gamma}$. These fixed-point connections were numerically computed in two ways, first with the package UMFUT of Doedel. We then independently verified the connections using the ode package LSODE. The method we use is to initialize the ode system with the coordinates of the unstable fixed points plus a small $(0(10^{-2}-10^{-3}))$ increment in the direction of the unstable eigenvector(s). The orbit then converges to the indicated fixed point. The only numerically sensitive connections are saddle-saddle connections, for which we impose tighter error bounds on the ode code and more careful resolution of the unstable manifold direction(s) to select initial conditions for the connecting orbit. The saddle-saddle connections are confirmed by restriction to the invariant subspace $b=0$, where the connections become saddle-stable node, which are numerically stable.

The interesting and relevant connections for this discussion are those for $\tilde{\Gamma}$ preceding and following the Hopf bifurcation at $\tilde{\Gamma}\approx .268$. We indicate these schematically in Fig. 9.

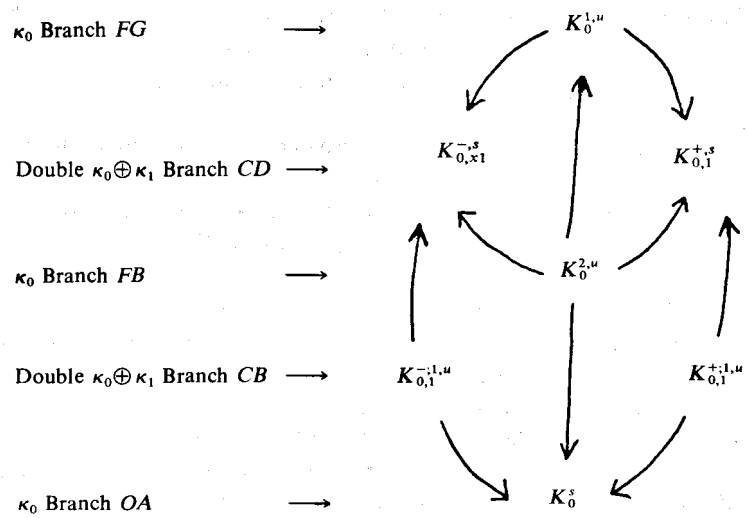

FIG. 9. *Global fixed-point connections* $.155<\tilde{\Gamma}<.268$.

These connections are quite expected from the pde. For example, the large amplitude unstable mean $(K_0^{1,u})$ is unstable to the nearest energy stable state, which is either the stable breather plus mean $(K_{0,1}^{+,s})$ or its equal energy translate $(K_{0,1}^{-,s})$. Thus, the unstable manifold of $K_0^{1,u}$ lands in one direction at $K_{0,1}^{+,s}$, in the other at $K_{0,1}^{-,s}$. Another example is the unstable breather plus mean $K_{0,1}^{+;1,u}$. Along perturbations which decrease energy, the state is unstable to the stable flat configuration (K_0^s) since there is not enough energy to sustain the spatial structure. If energy is increased, however, the state is unstable to the higher energy breather plus mean $K_{0,1}^{+,s}$, which is stable.

After the Hopf bifurcation $\tilde{\Gamma}\gtrsim .268$, all that changes in Fig. 9 is that the stable $K_{0,1}^{\pm;s}$ fixed points become two-dimensionally, weakly unstable,

$$K_{0,1}^{\pm;s} \xrightarrow[\text{Hopf}]{\text{after}} K_{0,1}^{\pm;2,u}.$$

We observe numerically, however, that the unstable trajectories out of $K_0^{1,u}$, $K_0^{2,u}$, and $K_0^{\pm;1,u}$ (which previously, Fig. 9, converges to $K_{0,1}^{\pm,s}$) now flow very near to $K_{0,1}^{+;2,u}$ or $K_{0,1}^{-;2,u}$, dominated by the $O(1)$ attracting directions (stable dimension two), but slowly build up the weak instabilities, leave this neighborhood, then quickly land back in a neighborhood of either $K_{0,1}^{+;2,u}$ or $K_{0,1}^{-;2,u}$. The dynamics of these odes depicts classic intermittent chaos: the "laminar" behavior is characterized by settling into a neighborhood of $K_{0,1}^{+;2,u}$ or $K_{0,1}^{-;2,u}$, and the intermittent chaotic bursts are associated with the flight out of the neighborhood of one and subsequent landing back into either of them.

In Fig. 10 we exhibit the time evolution for a selected orbit of the perturbed odes (2.5) at $\tilde{\Gamma} = .275$, which corresponds exactly to the $\varepsilon\Gamma = .103$ pde numerical experiments shown in § 1, Figs. 2 and 3. The initial condition of Fig. 10 is taken along the unstable manifold nearby $K_{0,1}^{+;2,u}$, which is directly into the conjectured strange attractor. For consistency, we also continue this numerical run to $t = 10{,}000$ (corresponding to $t \sim 70{,}000$ in the pde time units), and the run remained chaotic. The leading Lyapunov number was computed to be $2^{.17}$.

Motivated by our pde study in § 1 and the identification of homoclinic K_0 structures in the chaotic dynamics, we now seek the analogue of homoclinic crossings in these model odes. We have so far identified a parallel structure between this model problem and the pde: the upper $K_0^{1,u}$ fixed point corresponds to the K_0, order 1 unstable flat state, associated to the unperturbed homoclinic components; the $K_{0,1}^{\pm;2,u}$ fixed points correspond to breather plus nonzero mean states, phase shifted by a half period, which are neutrally stable in the unperturbed equation, but which develop weak instabilities due to the perturbation when $\tilde{\Gamma} \gtrsim .268$.

The perturbed pde as evidenced in Figs. 2(a) and 2(b), exhibits intermittent chaos characterized by a passage out of a "laminar" $K_0 \oplus K_1$ state, through the homoclinic K_0 state, and then back into another weakly unstable $K_0 \oplus K_1$ state. In this perturbed ode, this behavior corresponds to the schematic loop of Fig. 11.

In summary, our numerical studies of the ode and pde clearly suggest that the onset of observable chaos may be described by a jumping process between two weakly unstable coherent states. (These two states are related by a discrete symmetry, $(c, b) \to (c, -b)$ in the ode, and in the pde by a half-period translation from a state localized in the center or the ends of the spatial interval.) In the *unperturbed ode and pde systems*, homoclinic orbits have been identified which are homoclinic in the pde to x-independent, order 1 unstable periodic solutions while in the ode these orbits are homoclinic to the ring of fixed points, $|c| = 1$, $b = 0$. In each system, these orbits are homoclinic to degenerate solutions that intermediate the unperturbed spatially localized solutions. *Moreover*, in both the perturbed ode and pde systems, we have numerically correlated the jumping process with unperturbed homoclinic crossings.

It is therefore clear to us that a Melnikov-type calculation is appropriate, centered on the unperturbed homoclinic orbits. The goal of this analysis is to establish our conjecture for the observable chaotic dynamics: the existence of horseshoes in the perturbed dynamics, which rigorously identifies the jumping process in the ode and pde as topologically conjugate to a Bernoulli shift on two symbols. (The two symbols represent the states localized in the center and wings of the interval.)

A precise dynamical systems mechanism for the observable chaos has been formulated in collaboration with Wiggins and Kovacic. The ode scenario is based on existence of a four-dimensional Silnikov-like structure (Guckenheimer and Holmes [13, § 6.5], and Wiggins [14, § 3.2]); the rigorous proof is in progress by Wiggins and Kovacic and will appear in the thesis of Kovacic. The extension of this rigorous analysis to the pde is in progress [15].

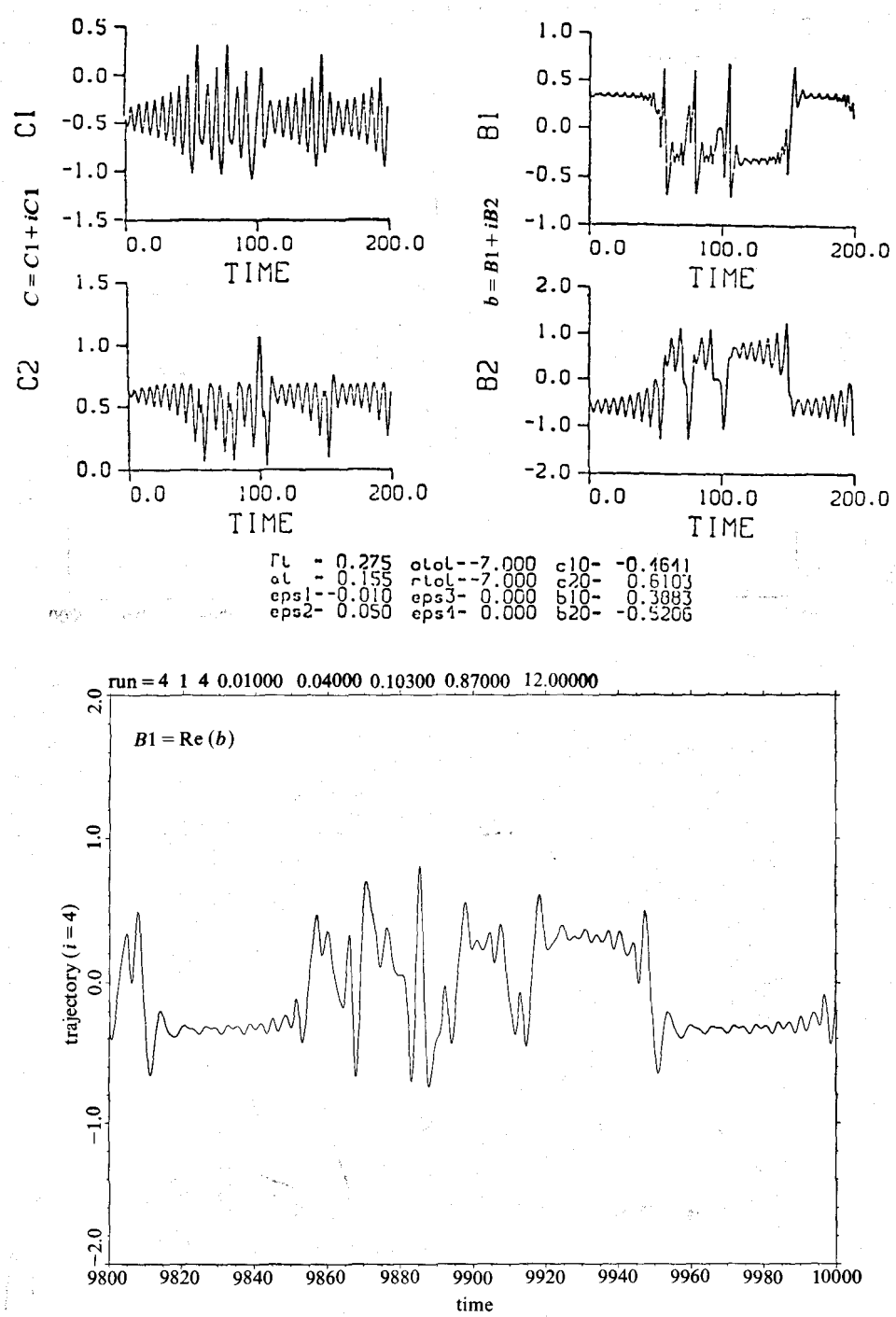

FIG. 10. *Time evolution of the odes* (2.5) *in the chaotic regime at* $\tilde{\Gamma} = .275$, *corresponding to the pde experiments of Figs.* 2 *and* 3 *at* $\epsilon\Gamma = .103$. *The initial condition for this time series is a small increment* $(0(10^{-2}))$ *from* $K_{0,1}^{+;2,u}$ *in the unstable eigendirections, chosen so that the flow immediately finds the surmised strange attractor. We also include one graph from this time series near* 10,000 *time units, comparable to the pde time series in Fig.* 2.

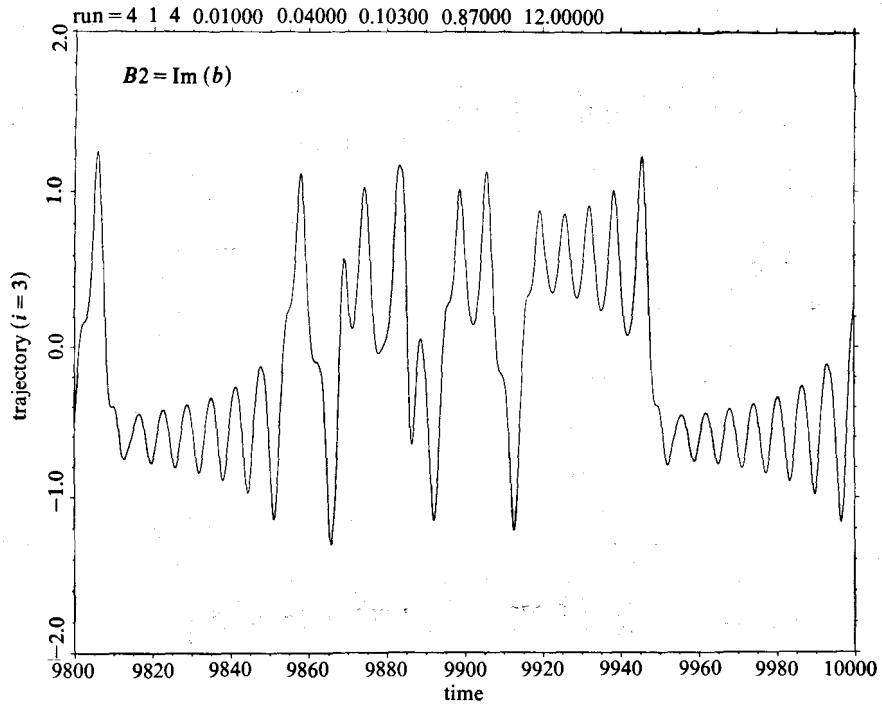

FIG. 10—continued

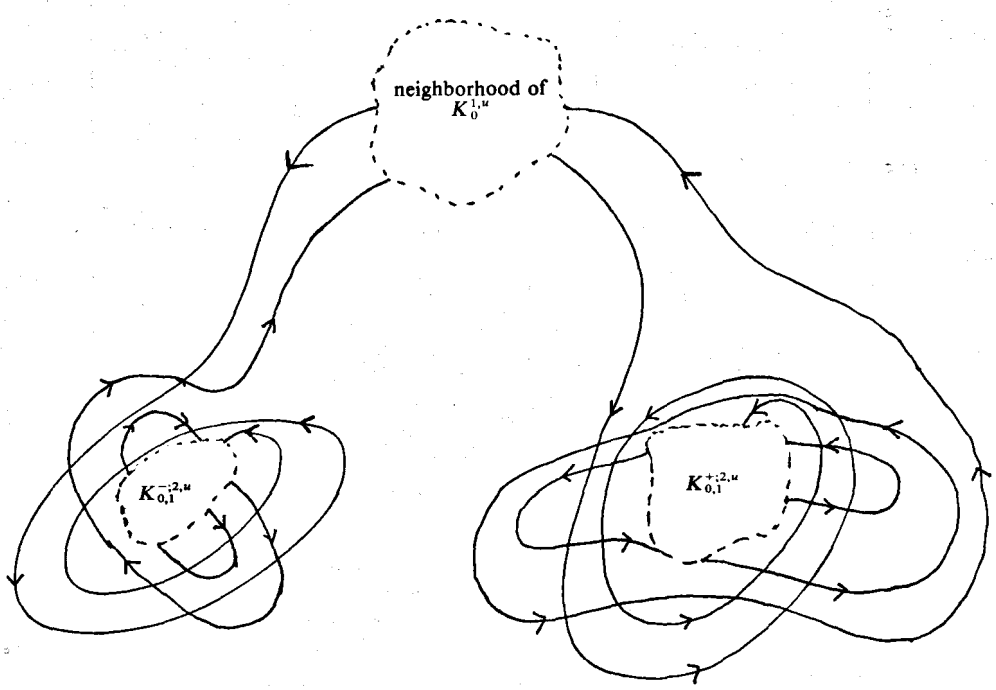

FIG. 11. *Schematic loop of behavior on the chaotic attractor.*

This surmised behavior creates a loop as sketched in Fig. 11. We test this conjecture numerically in the following way.

Starting at $K_{0,1}^{+;2,u}$ or $K_{0,1}^{-;2,u}$, we use the computed unstable eigenvectors to locally span $W_2^u(K_{0,1}^{\pm;2,u})$. We then numerically shoot from these fixed points $K_{0,1}^{\pm;2,u}$ along the unstable manifold, integrate the perturbed flow, and numerically monitor the distance to all fixed points at this value of $\tilde{\Gamma}$. These distance functions are defined as follows relative to the labeling in Fig. 12: DIS j = distance of the computed orbit to fixed point j, etc. These distance functions DIS 1–DIS 7 are provided below (Fig. 13) for one of the representative unstable eigendirections out of $K_{0,1}^{+;2,u}$, which coincides with the time evolution provided in Fig. 10.

Conclusion. The numerical evidence verifies the jumping process between neighborhoods of $K_{0,1}^{+;2,u}$ and $K_{0,1}^{-;2,u}$, with intermediate passages nearby $K_0^{1,u}$ during the jumps. Note that the DIS 2 and DIS 3 functions oscillate near zero as the orbit settles into a neighborhood of $K_{0,1}^{+;2,u}$ or $K_{0,1}^{-;2,u}$, respectively.

$K_0^{1,u} \equiv$ fixed point 1

$K_{0,1}^{+;2,u} \equiv$ fixed point 2 $\qquad$ $K_{0,1}^{-;2,u} \equiv$ fixed point 3

$K_0^{2,u} \equiv$ fixed point 4

$K_{0,1}^{+;1,u} \equiv$ fixed point 5 $\qquad$ $K_{0,1}^{-;1,u} \equiv$ fixed point 6

$K_0^{s} \equiv$ fixed point 7

FIG. 12. *For $\tilde{\Gamma} = .275$, the seven fixed points are assigned a numerical label: 1 is assigned to $K_0^{1,u}$, 2 is assigned to $K_{0,1}^{+;2,u}$, etc.*

Moreover, in the bursts out of these "laminar" states, the orbit gets relatively close to $1 = K_0^{1,u}$ (occasionally very close) as indicated in the graph of DIS 1, whereas the orbit is always $O(1)$ distance from fixed points 4, 5, 6, and 7. Thus, as in the pde simulations of § 1, the perturbed ode apparently goes chaotic coincidentally with random passages through or near the homoclinic structures of the unperturbed problem.

One final measurement of this thesis is the ode analogue of our sine-Gordon spectral projection of the perturbed pde (Fig. 2(b)). The homoclinic unperturbed fixed-point Ring 1 has the integral dependence $H = \frac{1}{2}I^2 - I$, so that $h = H - (\frac{1}{2}I^2 - I) = 0$ on the homoclinic orbit (recall Property 6 of § 3). We now seek to measure the projection of the perturbed flow, relative to this unperturbed homoclinic configuration, by checking for zero crossings of h. The graph of h is provided along with the distance functions in Fig. 13.

5. Correlations between the infinite-dimensional and reduced systems. So far, we have measured homoclinic crossings in two distinct ways: *in the perturbed* pde by graphing the exact sine-Gordon spectrum of u^ε at each timestep, and *in the* ode by graphing $h = H - (\frac{1}{2}I^2 - I)$ and checking for zero crossings. As a final test of this

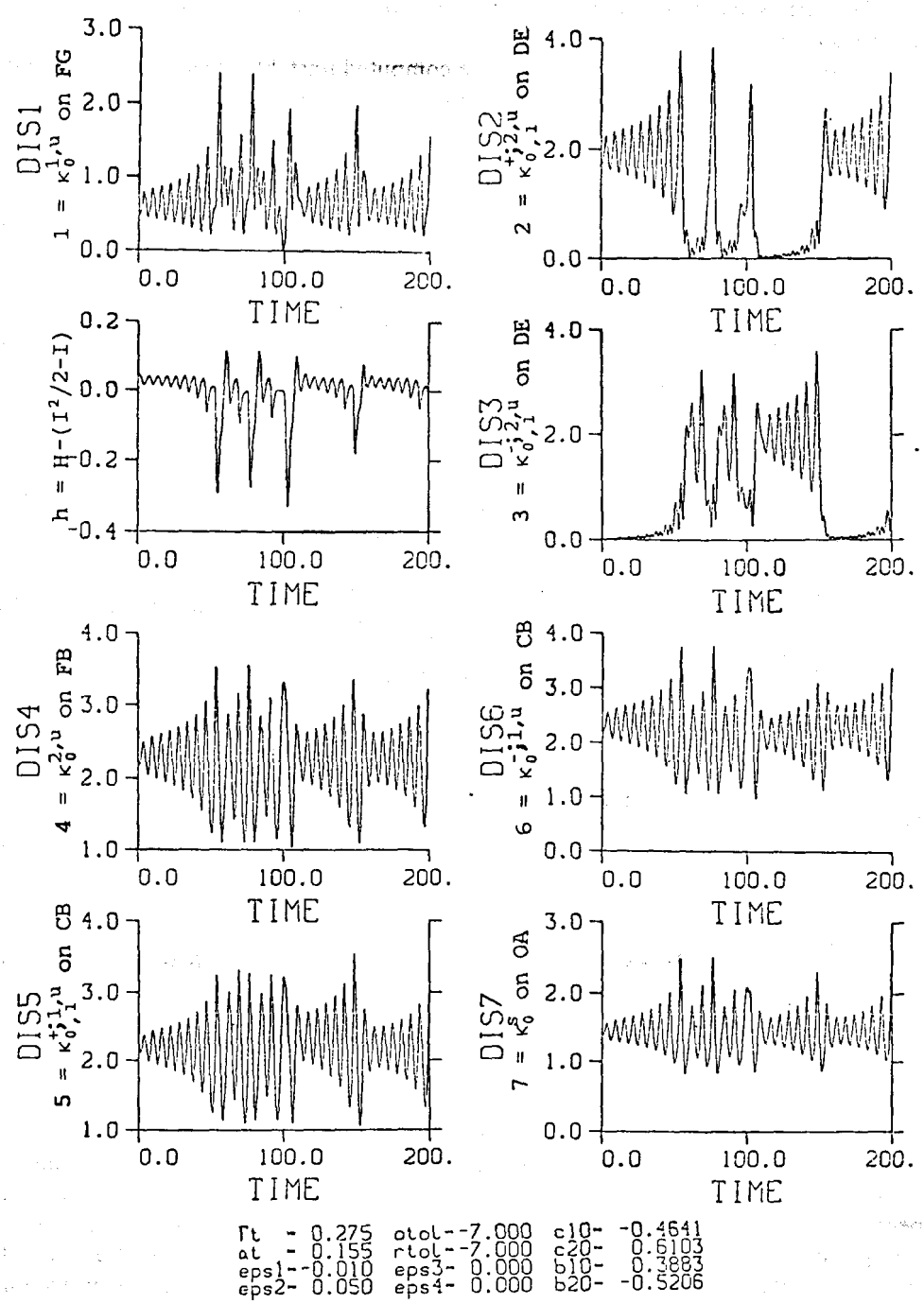

DISJ = distance from (c(T), b(T)) to fixed point J.

FIG. 13. *With the labeling of fixed points 1–7 as in Fig. 12 (fixed point* $1 = K_0^{1,u}$, *etc.), and with the orbit* $(c(t_n), b(t_n))$ *from Fig. 10 on the chaotic attractor, distance functions,* DIS j, $j = 1, \cdots, 7$, *are computed which measure the orbit point's distance to fixed point* j *at each timestep* t_n. *Importantly, note the changes in vertical scales.*

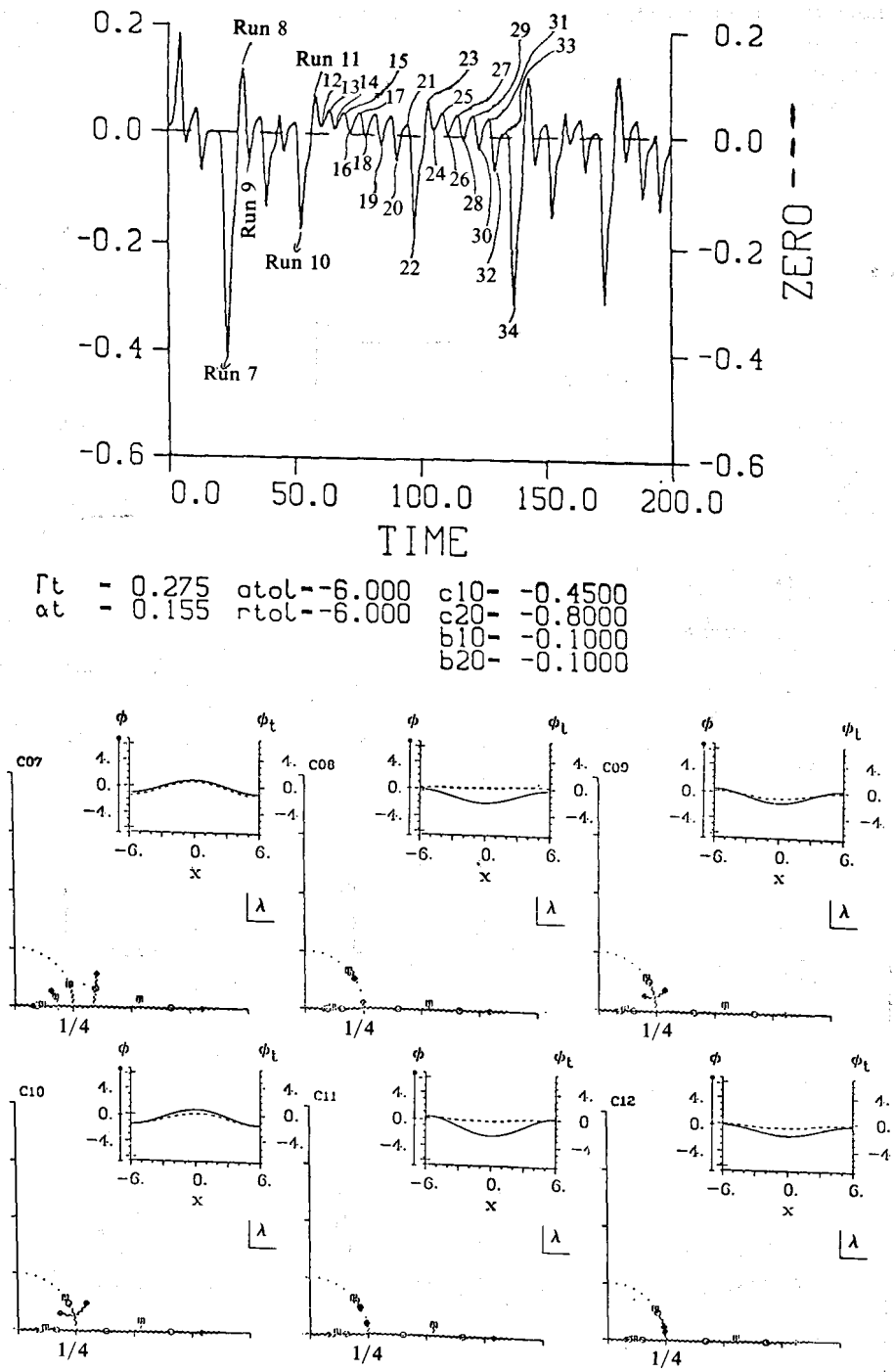

FIG. 14. *The ode and pde homoclinic diagnostics are computed together from an orbit* $(c(t_n), b(t_n))$ *on the chaotic attractor. The top graph is the ode diagnostic,* $h = H - (\frac{1}{2}I^2 - I)$, *which we check for zero crossings, with several discrete times labeled. From the values* $(c(t_n), b(t_n))$ *at these discrete times, the approximate perturbed sine-Gordon solution,* $u^\varepsilon(x, t_n)$, *is computed from formula* (2.1a). *Then the corresponding sine-Gordon spectral measurement of this approximate* u^ε *is computed. We then seek the correlation between zero crossings of the ode diagnostic h and passage through the homoclinic spectral configuration of the pde.*

homoclinic phenomenon, we combine the two measurements. We take $c(T_n)$, $b(T_n)$ during the flow that generates h, reconstruct the perturbed sine-Gordon solution u^ε by the approximation, (2.1a), and then compute the sine-Gordon spectral measurement of u^ε. When h goes through a zero crossing, does the perturbed sine-Gordon field u^ε pass through a homoclinic spectral configuration? The results appear in Fig. 14.

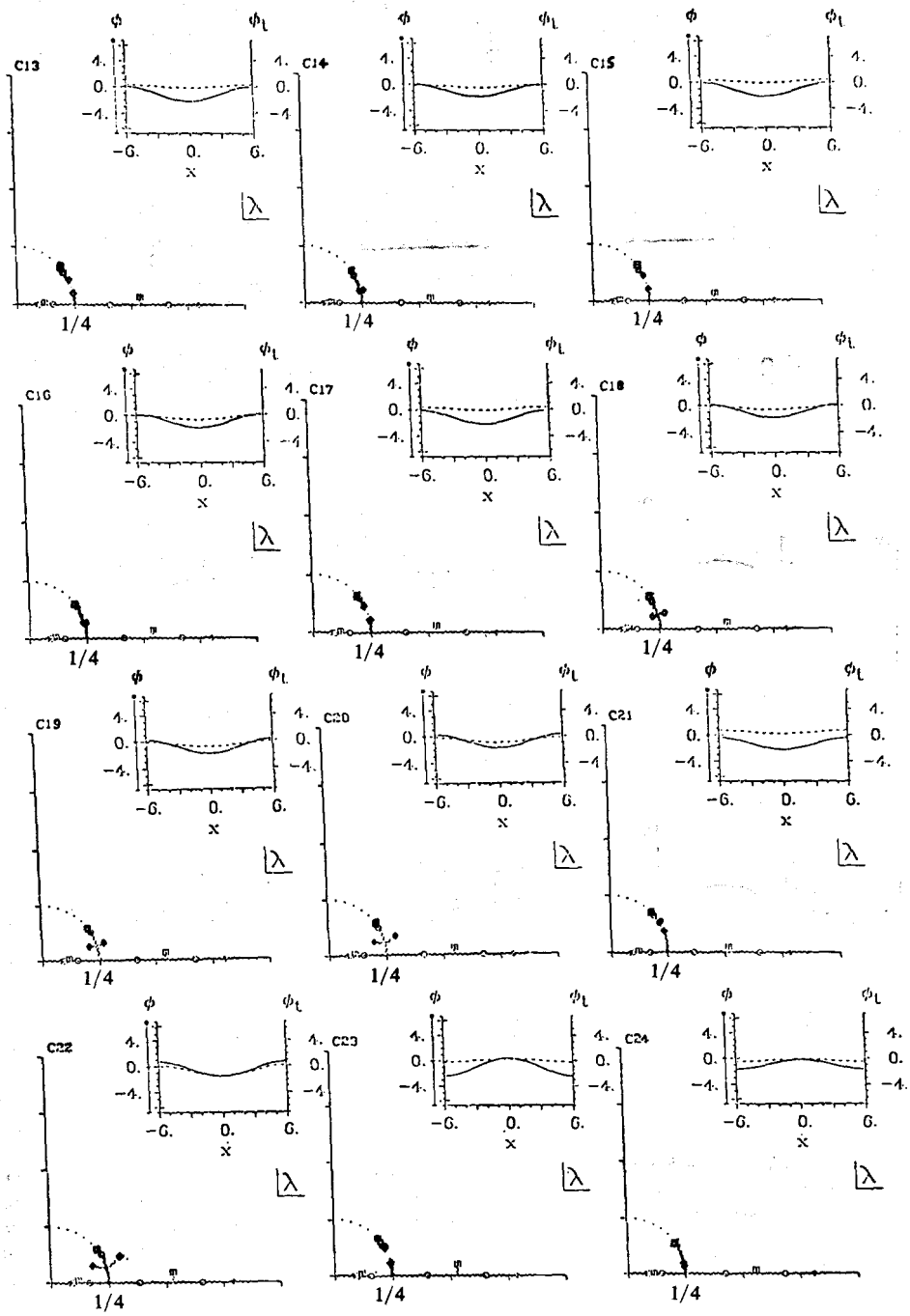

FIG. 14—continued

The agreement is quite good. When the odes pass from $h>0$ to $h<0$, the sine-Gordon projection goes from a "gap" to a "cross" configuration. The agreement is not one-to-one when the odes are very close to the exact homoclinic structure ($h \approx 0$), but this is expected due to the approximation by linear Fourier modes.

6. Concluding remarks. Based on the combination of:

(i) Our geometric understanding of the integrable sine-Gordon phase space, with singular components homoclinic to tori, and

(ii) The numerically verified presence of these singular components in the chaotic dynamics of the weakly perturbed system,

we are led to a research program to coordinatize these chaotic attractors and model the dynamics with associated amplitude equations. This paper represents the simplest example in the small amplitude limit of this general program. This two complex amplitude truncation has already yielded excellent correlation with the homoclinic structure that it shares with the perturbed integrable pde. Moreover, this "physically derived" four-dimensional dynamical system is a fertile example from the pure dynamical systems point of view. A Melnikov-type analysis based on the homoclinic orbits has now been developed for this model problem [4a], [4b], and will appear in the thesis of Kovacic.

The next step in this program is to truncate on the fully nonlinear sine-Gordon or nonlinear Schrödinger modes. Thus far, we have derived the averaged finite amplitude modal equations for systems (1.1) and (2.2), and have explicit formulas for the $K_0 \oplus K_1$ truncation relevant for the study presented here. (This analysis is discussed in [7].) The averaged equations are equivalent to the order ε rate of change for each sine-Gordon integral in the presence of the perturbation, i.e., $dH_j/dt = \varepsilon f_j, j \in Z$. These are precisely the quantities required in a Melnikov analysis in higher dimensions.

To capture the dynamics of the chaotic attractors, we must couple the rapid phases (the angles) to the averaged equations (the actions) described above. These perturbed action-angle equations will be reported in [5]. The next nontrivial step is to numerically analyze these truncated dynamical systems. Since these nonlinear coordinates are naturally defined on Riemann surfaces (see [3], [5]-[7]), we are currently developing efficient algorithms for these computations [8].

Appendix. Most of the numerical runs were done using a second-order in time, fourth-order in space discretization of the sine-Gordon pde (1.1). The u_{xx} term was discretized by fourth-order central differences with $\Delta x = 0.20$ and the u_t and u_{tt} terms were discretized by second-order central differences with $\Delta t = 0.02$ (i.e., this is a leapfrog scheme). The initial timestep was calculated by Taylor series, namely,

$$u(x, t=\Delta t) = u(x, 0) + u_t(x, 0)\Delta t + \tfrac{1}{2}u_{tt}(x, 0)(\Delta t)^2$$

and the u_{tt} term was replaced by using (1.1a). Selected runs were rechecked by a fourth-order Runge-Kutta method in time using eighth-order central differences in space (and the same Δx and Δt as above) on the pde to make sure that the long-time evolution of the run was as indicated by the lower-order method. In addition the boundaries between periodic and chaotic runs in time were determined to three decimal places by this higher-order code.

Acknowledgments. We express gratitude to Mac Hyman, Michael Jolly, and Yannis Kevrekides for generous numerical assistance. M. Gregory Forest and David W. McLaughlin also thank L. S. Young for helpful discussions. We all express gratitude to the Theoretical Division and Center for Nonlinear Studies, Los Alamos National Laboratories, Los Alamos, New Mexico, where this research was performed.

REFERENCES

[1] A. R. BISHOP, M. G. FOREST, D. W. MCLAUGHLIN, AND E. A. OVERMAN II, *A quasi-periodic route to chaos in a near-integrable pde*, Phys. D, 23 (1986), pp. 293-328, and references cited therein.

[2] A. R. BISHOP, D. W. MCLAUGHLIN, AND E. A. OVERMAN II, *Coherence and chaos in the driven, damped sine-Gordon equation: measurement of the soliton spectrum*, Phys. D, 19 (1986), pp. 1-41.

[3a] N. M. ERCOLANI, M. G. FOREST, AND D. W. MCLAUGHLIN, *Geometry of the Modulational Instability. Part* I: *Local Analysis*, Mem. Amer. Math. Soc., to appear.

[3b] ———, *Geometry of the Modulational Instability. Part* II: *Global Analysis*, Mem. Amer. Math. Soc., to appear.

[3c] ———, *Homoclinic orbits for the periodic sine-Gordon equation*, Phys. D, to appear.

[3d] ———, *The origin and saturation of modulational instabilities*, Phys. D, 18 (1986), pp. 472-474.

[4a] G. KOVACIC AND S. WIGGINS, preprint, California Institute of Technology, Pasadena, CA, 1988. Phys. D, submitted.

[4b] N. M. ERCOLANI, M. G. FOREST, AND D. W. MCLAUGHLIN, *Notes on Melnikov integrals for models of the driven pendulum chain*, preprint, University of Arizona, Tempe, AZ, 1988.

[5] ———, *Fully nonlinear modal equations for nearly integrable pdes*, preprint, Ohio State University, Columbus, OH, May 1988.

[6a] N. M. ERCOLANI, M. G. FOREST, D. W. MCLAUGHLIN, AND R. MONTGOMERY, *Hamiltonian structure of the modulation equations for sine-Gordon wavetrains*, Duke Math. J., 55 (1987), pp. 949-983.

[6b] M. G. FOREST AND D. W. MCLAUGHLIN, *Canonical variables of the periodic sine-Gordon equation and a method of averaging*, unpublished preprint, internal report of the Los Alamos National Laboratory, Los Alamos, NM, 1978.

[7] N. M. ERCOLANI, M. G. FOREST, AND D. W. MCLAUGHLIN, *Oscillations and instabilities in nearly integrable pdes*, Lectures in Appl. Math., 23 (1985), pp. 3-46.

[8] R. FLESCH, M. G. FOREST, AND A. SINHA, *Numerical inverse spectral transform for the periodic sine-Gordon equation: theta function solutions and their linearized stability*, Phys. D, submitted.

[9] E. OTT AND D. A. RUSSELL, *Chaotic (strange) and periodic behavior in instability saturation by the oscillating two-stream instability*, Phys. Fluids, 24 (1981), pp. 1976-1988.

[10] J. C. ARIYASU AND A. R. BISHOP, Phys. Rev. B, (3), (1987).

[11] A. R. BISHOP, M. G. FOREST, D. W. MCLAUGHLIN, AND E. A. OVERMAN II, *Quasiperiodic route to chaos in a near integrable P.D.E.: homoclinic crossings*, Phys. Lett. A, 127 (1988), pp. 335-340.

[12] D. W. MCLAUGHLIN, A. PEARLSTEIN, AND G. TERRONES, *Stability and bifurcation of time-periodic solutions of the damped and driven sine-Gordon equation*, preprint, University of Arizona, Tempe, AZ, May 1988.

[13] J. GUCKENHEIMER AND P. HOLMES, *Nonlinear Oscillations, Dynamical Systems, and Bifurcations of Vector Fields*, Appl. Math. Sci., Vol. 42, Springer-Verlag, Berlin, New York, 1983.

[14] S. WIGGINS, *Global Bifurcations and Chaos: Analytical Methods*, Appl. Math. Sci., Vol. 73, Springer-Verlag, Berlin, New York, 1988.

[15] N. M. ERCOLANI, M. G. FOREST, G. KOVACIC, D. W. MCLAUGHLIN, AND S. WIGGINS, work in progress.